Optimizing Interface Conductivity in Electronics

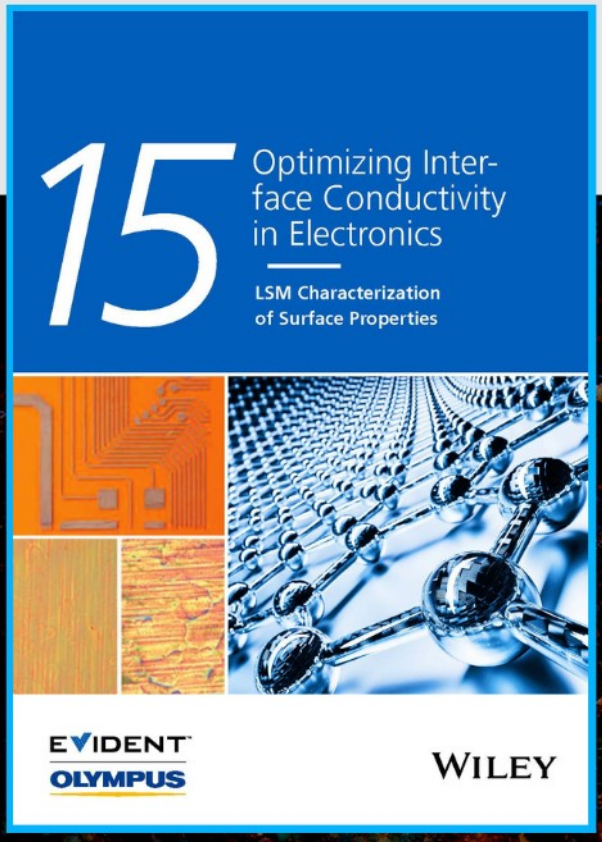

The latest eBook from Advanced Optical Metrology. Download for free.

Surface roughness is a key parameter for judging the performance of a given material's surface quality for its electronic application. A powerful tool to measure surface roughness is 3D laser scanning confocal microscopy (LSM), which will allow you to assess roughness and compare production and finishing methods, and improve these methods based on mathematical models.

Focus on creating high-conductivity electronic devices with minimal power loss using laser scanning microscopy is an effective tool to discern a variety of roughness parameters.

EVIDENT
OLYMPUS

WILEY

ADVANCED FUNCTIONAL MATERIALS
www.afm-journal.de

Microneedle Patch Integrated with Porous Silicon Confined Dual Nanozymes for Synergistic and Hyperthermia-Enhanced Nanocatalytic Ferroptosis Treatment of Melanoma

Jingwen Zhao, Wei Duan, Xingyue Liu, Fengna Xi, and Jianmin Wu**

Superficial melanoma is the deadliest form of skin cancer without desirable clinically therapeutic options. Nanozymes, artificial nanomaterials with physicochemical performance and enzyme catalytic properties, have attracted considerable attention for antitumor therapy. However, the therapeutic efficiency of nanozymes is vulnerable to the tumor microenvironment (TME) and delivery process. Herein, a microneedle (MN) patch that integrates porous silicon (PSi) loaded with dual nanozymes is devised to bidirectionally regulate TME and accurately deliver nanocomplex to initiate ferroptosis for melanoma treatment. Benefitting from the channel confinement effect of PSi, the copper-doped graphene quantum dots and palladium nanoparticles coloaded PSi (CuGQD/PdNPs@PSi) exhibit synergistic effect with enhanced mimicking peroxidase and glutathione oxidase activities, which are ≈2–3-fold higher than those of monoconfined nanozyme or nonconfined nanozyme complexes. Additionally, the synergistic catalytic performance of CuGQD/PdNPs@PSi can be improved via photostimuli hyperthermia. The CuGQD/PdNPs@PSi can induce ferroptosis manifested by upregulation of lipid peroxides and inactivation of glutathione peroxidase 4. Furthermore, loading of nanocomplexes into MNs for administration resulted in a satisfactory melanoma growth inhibition of 98.8% within 14 days. Therefore, MNs encapsulated with CuGQD/PdNPs@PSi can provide a potentially nanocatalytic strategy for ferroptosis-inducing tumor treatment while also meeting the medical needs of eradicating superficial tumors.

1. Introduction

More than one million cases of skin cancer are diagnosed annually worldwide and the prevalence has increased over the past few decades.[1,2] Cutaneous melanoma (CM) is a highly malignant tumor with 80% of skin cancer fatalities. CM differs from other malignant tumors in that it mainly occurs in the skin's epidermis and dermis rather than deep tissue.[3–5] One vital reason for the high mortality caused by CM is the lack of reliable and efficient therapeutic methods. The surgical excision of superficial lesions and adjacent skin tissues has been the primary standard treatment of melanoma.[6] However, surgical resection is associated with a lengthy recovery period and the patient's susceptibility to infection. Typical chemotherapy will inevitably result in drug resistance and adverse health repercussions.[7] Immunotherapy is a novel therapeutic approach, but the problems of therapeutic complexity and the long-term viability of recoded cells need to be addressed.[8] In addition, low DNA damage and numerous DNA repairs in melanoma render it resistant to radiotherapy.[9] Hence, developing innovative and effective melanoma therapy approaches is crucial to increase patient survival rates.

The emergence of nanoformulation has provided an alternative and prospective therapy for tumor treatment. In recent years, nanozymes exhibiting similar enzymatic kinetics to natural enzymes under physiological conditions have been extensively exploited.[10] It has been well known that tumor microenvironment (TME) is distinctive from normal tissues in the aspects of nutrient deficiency, hypoxia, weakly acidic pH, immunosuppression, and overexpression of hydrogen peroxide (H_2O_2) and glutathione (GSH).[11,12] These traits promote the metabolism and proliferation of tumor cells and eventually lead to the uncontrolled progression of tumors. Interestingly, in contrast to the passive or active tumor targeting of other nanoformulations, the nanozymes can target the characteristic metabolites of TME to induce the catalytic therapy. With endogenous stimulation of the

J. Zhao, W. Duan, X. Liu, J. Wu
Lab of Nanomedicine and Omic-based Diagnostics
Institute of Analytical Chemistry
Department of Chemistry
Zhejiang University
Hangzhou 310058, P. R. China
E-mail: wjm-st1@zju.edu.cn

F. Xi
Key Laboratory of Surface & Interface Science of Polymer Materials of Zhejiang Province
School of Chemistry and Chemical Engineering
Zhejiang Sci-Tech University
Hangzhou 310018, P. R. China
E-mail: fangnaxi@zstu.edu.cn

The ORCID identification number(s) for the author(s) of this article can be found under https://doi.org/10.1002/adfm.202308183

DOI: 10.1002/adfm.202308183

TME, nanozymes can induce the conversion or breakdown of endogenous substances to attack cancer cells or disrupt the internal equilibrium of TME and ultimately inhibit the tumor development. For example, peroxidase (POD)-mimicking nanozymes can catalyze the decomposition of H_2O_2 to produce hydroxyl radicals (•OH), which can induce DNA damage and protein denaturation of tumor cells.[13] The nanozyme with POD mimicking activity include noble metal nanoparticles, metal oxide, and carbon nanomaterials (e.g., carbon nanotubes, fullerene, and graphene quantum dots (GQD).[14–16] Glutathione oxidase (GSHOx) mimicking nanozymes usually contain highly oxidized metal elements (Cu(II),[17,18] Mn(IV),[19] and V(V)[20]), which could convert supernormal GSH to GSSG for reducing the antioxidant stress capacity of cancer cells via a redox reaction.[21] More importantly, nanozymes with both POD and GSHOx properties can produce •OH for oxidation of lipid peroxide (LPO) and simultaneously inactivate glutathione peroxidase 4 (GPx-4) by consuming GSH to induce irreversible LPO, which could effectively trigger ferroptosis featuring accumulation of LPO.[21,22]

Additionally, nanozymes with the ability of responding to external stimuli (light, heat, ultrasound, etc.) have been used for multimodal tumor therapy. Exogenous stimulation could endow nanozymes with additional photodynamic effect, photothermal effect, and sonodynamic effect to further enhance the therapeutic properties. For example, hyperthermia induced by localized photothermal therapy (PTT) can significantly improve the antitumor efficacy of nanozymes through accelerating the nanocatalytic reaction in endogenous TME.[23,24]

Therefore, much effort has been devoted to developing highly active nanozyme systems that can simultaneously target multiple TME metabolic pathways and respond to external stimuli.

Coloading nanozyme into carriers is a promising approach to construct multimodel antitumor platform to target complex TME. Up to now, a variety of materials have been developed as nanozyme carriers including graphene,[25] transition metal disulfide,[26] and mesoporous silica nanospheres (MSN).[27] Compared with these nanocarriers, electrochemical etched porous silicon (PSi) with tunable mesopore channel and active surface chemistry is highly compatible to loading nanomaterials.[28,29] Moreover, the PSi nanocarrier displays drug protective effect, higher biocompatibility, and high biodegradability than MSN carrier.[30] The degradation product of PSi in vivo is orthosilicic acid ($Si(OH)_4$), which is not hazardous to organisms and could be quickly metabolism and renal clearance.[31] At present, the PSi-based drug and nanocomposite system have been employed in various biomedical applications, including biosensors,[32,33] wound healing,[34,35] antimicrobial treatment,[28,36,37] and chemotherapy for cancer.[38,39] Our previous works have demonstrated that noble metal nanoparticles (sliver nanoparticles (AgNPs), gold nanoparticles (AuNPs)), carbon quantum dots, and GQD can be effectively coloaded in PSi host to construct optical nanosensor and therapeutic platform.[28,33,40] However, coloading dual nanozymes and confinement effect of PSi on the stimuli-response and synergistic catalytic activity of multiple nanozymes still needs to be investigated.

Herein, PSi carrier was first used to coload dual nanozymes and then integrated into microneedles (MNs) for synergistic nanocatalytic and hyperthermia-enhanced ferroptosis treatment against cutaneous melanoma (**Figure 1**). Palladium nanoparticles (PdNPs) have been reported as a special noble metal with both mimic-POD nanozymatic properties and photothermal properties for bimodal tumor treatment.[41,42] By utilizing the reducibility of Si—H bond on the fresh-etched PSi, PdNPs can be easily loaded on PSi surface by in situ reduction of metal salt to obtain PdNPs@PSi. Additionally, Cu(II)-doped carbon nanomaterials are promising candidates for simultaneous mimicking of POD and GSHOx.[43,44] Therefore, we used copper-doped graphene quantum dots (CuGQD) as an alternative type of nanozyme for further loading into PdNPs@PSi. The dual nanozymes coloaded PSi (CuGQD/PdNPs@PSi) possesses desirable PTT activity and mimicking POD and GSHOx feature. Especially, owing to the pore confinement effect, the dual nanozymes exhibit prolonged and synergistic catalytic performance as well as improved hyperthermia, resulting in higher ROS production and efficient elimination of overexpressed GSH to induce the ferroptosis of tumor cells. Moreover, the integration of CuGQD/PdNPs@PSi in MNs allows the coloaded nanozymes to penetrate the epidermal barrier and administrate to the dermis where melanoma is primarily located owing to the formation of reversible microchannels.[45,46] Consequently, the MNs integrated with CuGQD/PdNPs@PSi showed excellent antitumor effects in vivo due to their enzymatic activity targeting to the TME of melanoma, eventually resulting in ferroptosis. The MNs integrated with multiple nanozymes coloaded into PSi hold great potential for highly efficient superficial tumor therapy ascribing to its stimuli-response and interplay between the nanozymes confined into pore channel.

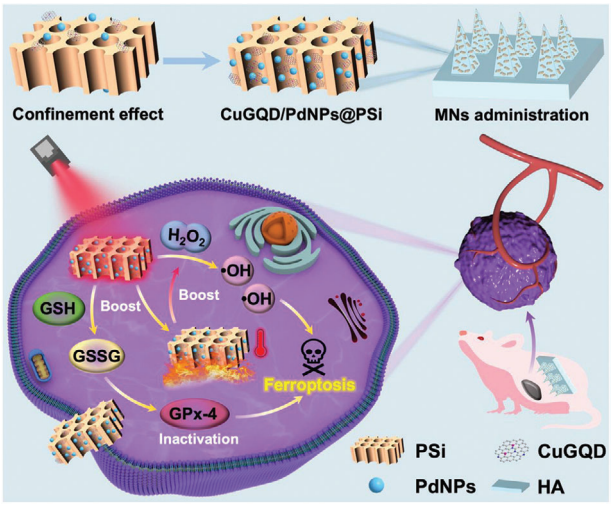

Figure 1. Schematic illustration of microneedle integrated with PSi loaded with bifunctional nanozymes (including copper-doped graphene quantum dots (CuGQD) and palladium nanoparticles (PdNPs)) to induce ferroptosis of subcutaneous melanoma through nanocatalytic strategy.

2. Results and Discussion

2.1. Synthesis and Characterization of CuGQD/PdNPs@PSi

The preparation procedure of CuGQD and PdNPs coloaded nanoscale PSi (CuGQD/PdNPs@PSi) is illustrated in **Figure 2**a. Generally, the typical electrochemical etching method was used

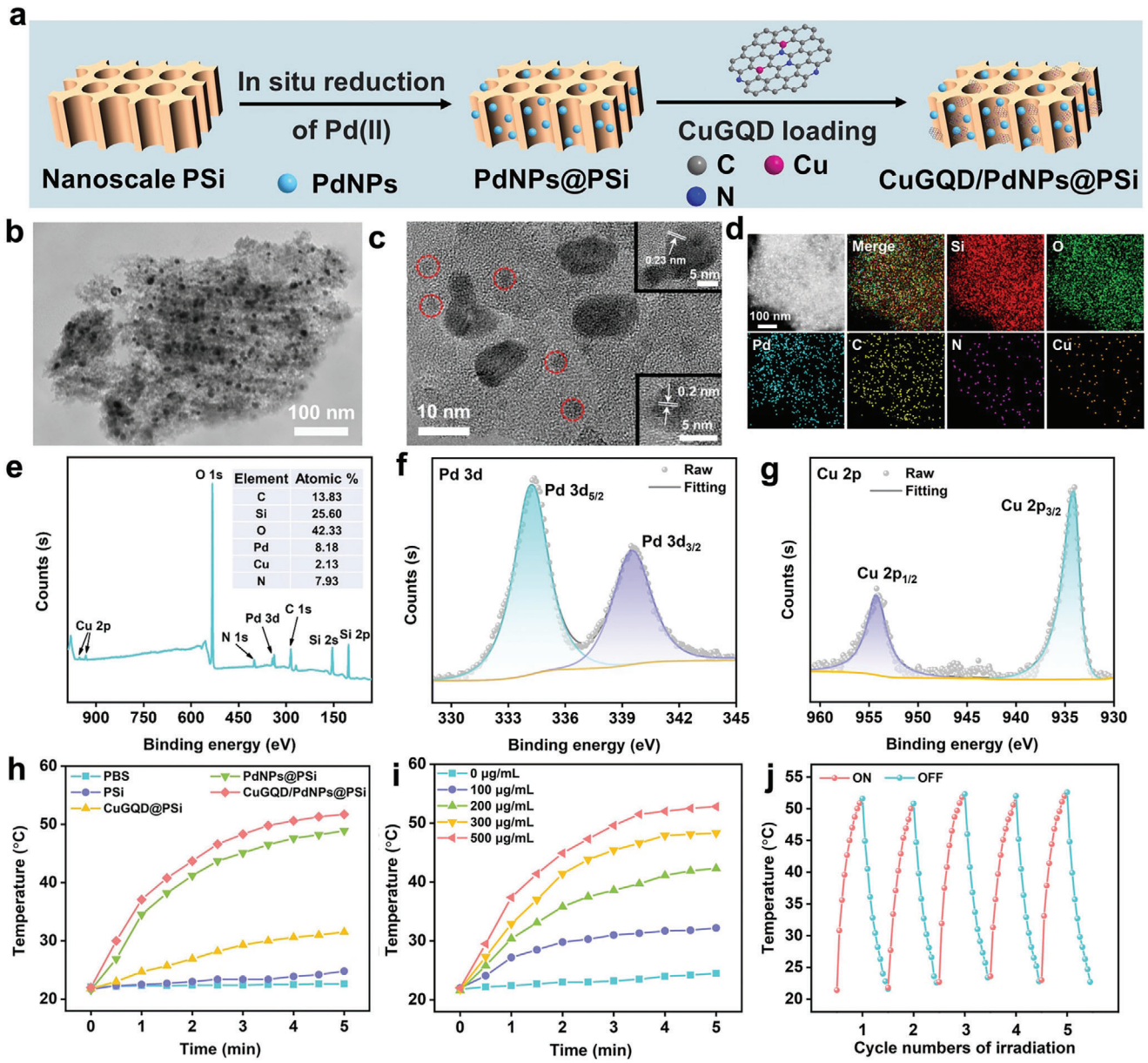

Figure 2. Synthesis and characterization of CuGQD/PdNPs@PSi. a) Schematic illustration of the fabrication of CuGQD/PdNPs@PSi. b) TEM image of CuGQD/PdNPs@PSi. c) HRTEM images of CuGQD/PdNPs@PSi. The red circle represents CuGQD. Insets are the HRTEM image of PdNPs (upper) and CuGQD (bottom) in PSi host. d) Elemental mappings of CuGQD/PdNPs@PSi. e–g) XPS survey spectrum of CuGQD/PdNPs@PSi (e) and high-resolution Pd 3d (f) and Cu 2p (g) spectra of CuGQD/PdNPs@PSi. Photothermal response curves of h) different materials and i) CuGQD/PdNPs@PSi with different concentrations under NIR irradiation (808 nm, 1.0 W cm^{-2}). j) Temperature change curves of CuGQD/PdNPs@PSi upon exposure to NIR irradiation for 5 cycles.

to prepare PSi film, which was subsequently fractured by ultrasonic treatment to obtain nanoscale PSi. The nanoscale PSi produced by top-down ultrasonic fragmentation are ≈200–350 nm in size and show good porous structure and dispersion (Figure S1, Supporting Information). Then Pd(II) salt could be in situ reduced using PSi to obtain PdNPs loaded PSi (PdNPs@PSi) owing to the abundant reactive Si—H bonds from the nanoscale PSi. Compared with solution based methods for noble metal nanoparticles preparation, this unique in situ reduction and loading process can prevent the aggregation of PdNPs without using any protection agents. In addition, the surface reduction process is very quick, taking 1 min to complete the saturate loading of PdNPs as indicated in the equilibrium curve of photothermal response (Figure S2a, Supporting Information). Moreover, the photothermal characteristic of PdNPs@PSi is superior to PdNPs produced with high temperature reduction and polyvinylpyrrolidone protection (Figure S2b, Supporting Information). Subsequently, CuGQD was prepared by one-step hydrothermal method, then CuGQD and PdNPs@PSi were mixed and shaken for 2 h, and CuGQD/PdNPs@PSi were obtained after

centrifugation to remove uncombined CuGQD. High-resolution transmission electron microscope (HRTEM) and atomic force microscope (AFM) image reveal the average size of CuGQD is 3.0 nm (the lattice parameter is 0.21 nm, corresponding to the (102) plane of graphene[47]), and the thickness of CuGQD is ≈1.3 nm (Figure S3a,b, Supporting Information). X-ray photoelectron spectroscopy (XPS) manifests that the Cu element has been successfully doped in GQD (Figure S3c, Supporting Information). Moreover, the Cu 2p high-resolution spectrum exhibits two peaks at 934.1 and 954.3 eV,[48,49] indicating that Cu(II) is the primary form of CuGQD (Figure S3d, Supporting Information).

The zeta potential of PSi is -31.6 ± 0.9 mV, which is originated from the dissociation of Si-OH (p*Ka* = 2.0) on the mild oxidized PSi surface, while the zeta potential of CuGQD is $+8.21 \pm 0.2$ mV due to the dopping of positively charged copper ions. After loading CuGQD, the zeta potential of PSi is partially neutralized, leading to the less negative zeta potential of CuGQD@PSi ($\zeta = -23.8 \pm 0.1$ mV). The results indicate that electrostatic interaction is the main driving force for binding the CuGQD with PSi. The zeta potential of CuGQD/PdNPs@PSi is -21.2 ± 0.5 mV, which is less negative than that of PdNPs@PSi (-31.9 ± 0.6 mV) and PSi, suggesting that CuGQD is also combined with PSi or PdNPs@PSi through electrostatic adsorption (Figure S4, Supporting Information). The scanning electron microscope (SEM) image indicates the ordered nanochannels of CuGQD/PdNPs@PSi (Figure S5, Supporting Information). Transmission electron microscope (TEM) image (Figure 2b) exhibits the distribution of PdNPs with larger size (average size = 8.34 ± 1.63 nm) and higher contrast compared to CuGQD in the PSi channel. Figure 2c shows the presence of face-centered cubic (111) PdNPs crystal planes with lattice spacings of 0.23 nm in CuGQD/PdNPs@PSi.[50,51] The lattice spacing of CuGQD in the CuGQD/PdNPs@PSi is 0.2 nm, which is consistent with individual CuGQD (Figure 2c insets). The elemental mapping images of CuGQD/PdNPs@PSi reveal the homogenous distribution of Si, O, Pd, C, N, and Cu (Figure 2d). Furthermore, the XPS spectra also prove the presence of the above elements in CuGQD/PdNPs@PSi (Figure 2e). As shown in Figure 2f, two peaks locate at 339.5 and 334.2 eV correspond to the 3d5/2 and 3d7/2 of Pd (0), while no peaks of Pd(II) are found at 337 and 342.1 eV.[52] The high-resolution Cu 2p spectrum of CuGQD/PdNPs@PSi is consistent with the CuGQD (Figure 2g). Besides, the average pore volume measured by Brunauer–Emmett–Teller test is calculated to be 2.102 $cm^3 g^{-1}$ for the nanoscale PSi with pore size of 15.8 nm, indicating the characteristic mesoporous structure. By contrast, the average pore volume of CuGQD/PdNPs@PSi decreases to 0.6519 $cm^3 g^{-1}$ with pore size of 5.84 nm (Figure S6, Supporting Information). The results indicate that PdNPs and CuGQD are mainly loaded into the pore channels of PSi. Furthermore, the loading amounts of dual nanozymes in PSi host were also investigated. The amount of loaded PdNPs in CuGQD/PdNPs@PSi measured by inductively coupled plasma optical emission spectrometry is ≈129.4 ± 4.640 μg mg^{-1}, while the amount of loaded CuGQD quantified by fluorescence intensity of CuGQD is calculated to be 42.00 ± 1.793 μg mg^{-1} (Figure S7, Supporting Information). All the above results confirm that PdNPs and CuGQD have been successfully coencapsulated in PSi host. With increasing of storage time (0, 7, 14 days), the CuGQD/PdNPs@PSi display negligible aggregation or morphological changes, demonstrating the storage stability of CuGQD/PdNPs@PSi (Figure S8, Supporting Information).

2.2. The Photothermal Performance of CuGQD/PdNPs@PSi

The photothermal property of CuGQD/PdNPs@PSi was investigated under the irradiation of an 808 nm laser (1.0 W cm^{-2}, 5 min). The temperature of PSi solution and CuGQD@PSi solution can be increased by only ≈3 and ≈10 °C during the NIR laser irradiation, while the temperature in PdNPs@PSi and CuGQD/PdNPs@PSi system increases from 22 to 49 and 52 °C, respectively (Figure 2 h; Figure S9, Supporting Information), indicating that the introduction of PdNPs in the nanocomposite obviously improved the photothermal conversion ability. The photothermal response of CuGQD/PdNPs@PSi is superior to that of PdNPs@PSi due to the fact that the higher absorption of CuGQD/PdNPs@PSi than that of PdNPs@PSi at the same concentration (500 μg mL^{-1}) in full-coverage region of NIR and UV–vis (Figure S10, Supporting Information). CuGQD/PdNPs@PSi further display elevated temperature with increasing concentration and irradiation time (Figure 2i). Additionally, the temperature increase of CuGQD/PdNPs@PSi remains stable after 5 cycles of irradiation, indicating the high photostability of CuGQD/PdNPs@PSi (Figure 2j). The photothermal conversion efficiency (η) of CuGQD/PdNPs@PSi is calculated to be 57.8% (Figure S11, Supporting Information), which is significantly better than other Pd-based photothermal agents that have been reported (Table S1, Supporting Information).

2.3. The Nanocatalytic Activity of CuGQD/PdNPs@PSi

Nanozymes with mimic-POD performance can induce the decomposition of overexpressed H_2O_2 in endogenous TME to produce highly toxic •OH, which could cause tumor cell necrosis or apoptosis. This type of ROS-mediated nanozyme-based catalysis is of great clinical value for cancer treatment. Accordingly, we first investigated the mimic-POD activity of CuGQD/PdNPs@PSi in the slightly acidic TME environment (pH = 6.5). The colorimetric reaction of 3,3′,5,5′-tetramethylbenzidine (TMB) was used to study the POD-like property. Generally, POD can catalyze the decomposition of H_2O_2 to produce •OH, which can oxidize TMB to generate oxidation product (oxTMB) with a characteristic absorption (652 nm). After introducing CuGQD/PdNPs@PSi into the mixture of H_2O_2 and TMB, the reaction last for 5 min at the normal physiological temperature of 37 °C. The absorbance value of oxTMB is higher than that when using CuGQD@PSi or PdNPs@PSi as catalyst (Figure 3a). The steady-state kinetics of mimic-POD were analyzed using a typical Michaelis–Menten equation to obtain the Michaelis constant (K_m) and the maximum reaction rate (V_{max}) (Figure 3b,c). The CuGQD/PdNPs@PSi possess a lower K_m value (0.9735 mM) and higher V_{max} value (5.417×10^{-8} M s^{-1}) than that of CuGQD@PSi and PdNPs@PSi (Table S2, Supporting Information). Additionally, the V_{max}/K_m value was calculated, which could reflect the catalytic efficiency of the enzyme. As shown in Table S2 of the Supporting Information, CuGQD/PdNPs@PSi exhibit an ≈5-fold higher catalytic efficiency than CuGQD@PSi and ≈2.6-fold than PdNPs@PSi,

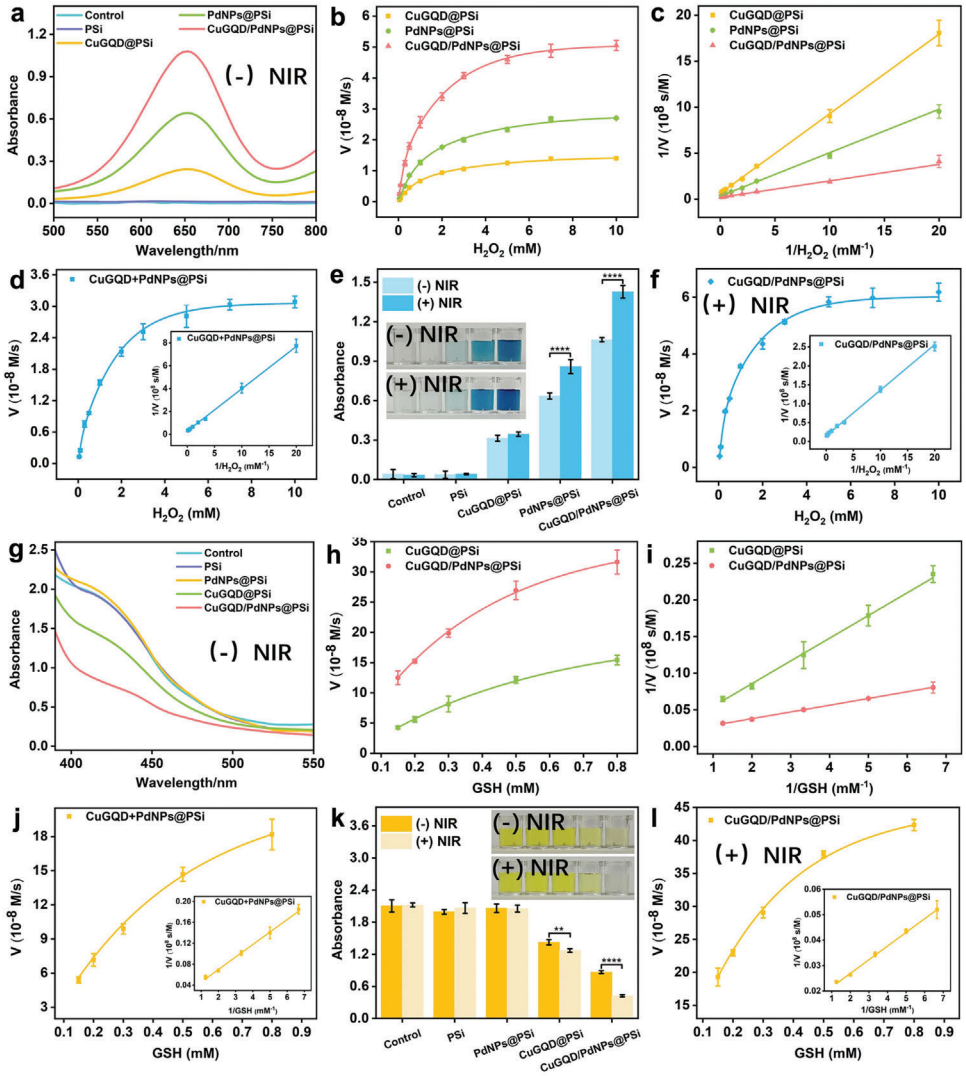

Figure 3. Evaluation of POD-mimic and GSHOx-mimic activities. a) Absorption spectra when different nanomaterials react with H_2O_2 and TMB at 37 °C for 5 min. b) Michaelis–Menten kinetic analysis and c) Lineweaver–Burk plot of CuGQD@PSi, PdNPs@PSi, and CuGQD/PdNPs@PSi with H_2O_2 as a substrate at 37 °C without NIR irradiation. d) Michaelis–Menten kinetic analysis and (inset) Lineweaver–Burk plot of CuGQD + PdNPs@PSi mixture with H_2O_2 as a substrate. e) Comparison of absorbance values of different materials reacting with H_2O_2 and TMB in the absence or presence of NIR light for 5 min ($n = 3$). Insets show photographs taken after the reaction in presence of different materials (from left to right: Control, PSi, CuGQD@PSi, PdNPs@PSi, and CuGQD/PdNPs@PSi) with or without NIR exposure. f) Michaelis–Menten kinetic analysis and (inset) Lineweaver–Burk plot of CuGQD/PdNPs@PSi with H_2O_2 as a substrate at 50 °C induced by NIR irradiation. g) Absorption spectra of different materials reacting with GSH and DTNB at 37 °C for 5 min. h) Michaelis–Menten kinetic analysis and i) Lineweaver–Burk plot of CuGQD@PSi and CuGQD/PdNPs@PSi with GSH as a substrate at 37 °C. j) Michaelis–Menten kinetic analysis and (inset) Lineweaver–Burk plot of CuGQD + PdNPs@PSi mixture with GSH as a substrate. k) Comparison of absorbance values obtained after different materials reacts with GSH and DTNB in the absence or presence of NIR light for 5 min ($n = 3$). Insets show photographs taken after the reaction of different materials (from left to right: Control, PSi, PdNPs@PSi, CuGQD@PSi, and CuGQD/PdNPs@PSi) without or with NIR stimulation. l) Michaelis–Menten kinetic analysis and (inset) Lineweaver–Burk plot of CuGQD/PdNPs@PSi with GSH as a substrate at 50 °C induced by NIR irradiation. Significance level was defined as *($p < 0.05$), **($p < 0.01$), ***($p < 0.001$), ****($p < 0.0001$).

proving that the coloading of dual nanozymes in PSi exhibits enhanced adsorption capacity to substrates and faster catalytic reaction rates. Electron spin resonance spectroscopy also confirmed that CuGQD/PdNPs@PSi could produce more •OH via Fenton-like reaction than CuGQD@PSi and PdNPs@PSi (Figure S12, Supporting Information).

Moreover, in order to clarify the synergistic catalysis mechanism, we added the same amount of CuGQD (42 µg) as in CuGQD/PdNPs@PSi to PdNPs@PSi solution without shaking to obtain the mixture of CuGQD and PdNPs@PSi. In this situation, we call this mixture as monoconfined nanozyme mixture because the majority of the CuGQD is in the free state, while the PdNPs exist in the confined state. The above mixture was analyzed for steady-state kinetics using H_2O_2 as a substrate. Compared with dual confined nanozymes complex CuGQD/PdNPs@PSi, the V_{max}/K_m value of monoconfined

nanozyme mixture is reduced by almost half (Figure 3d; Table S2, Supporting Information) with increased K_m value (1.311 мм) and decreased V_{max} value (3.545×10^{-8} м s^{-1}). The results indicate that the POD catalytic efficiency of dual confined nanozymes complex is significantly superior to that of monoconfined nanozyme mixture. This phenomenon can be attributed to two aspects: first, the PSi host ensures that the catalytic reaction is confined to the nanoscale pores, thus enhancing the binding rate to substrates and preventing the diffusion-limited kinetic as occurred in free state. Second, the dual confined nanozymes hosted in PSi may facilitate the electron transfer between the nanozymes, thus accelerating the redox catalytic reaction. Further, we used the slightly alkaline PBS solution (pH = 7.4) to destroy the PSi channel structure of CuGQD/PdNPs@PSi via oxidative degradation to obtain CuGQD/PdNPs (Figure S13, Supporting Information),[36] and then the steady-state kinetic study was carried out on CuGQD/PdNPs in the absence of the PSi channel. the K_m value and V_{max} value of CuGQD/PdNPs are 1.109 мм and 3.416×10^{-8} м s^{-1}, respectively (Figure S14 and Table S2, Supporting Information). The V_{max}/K_m value of CuGQD/PdNPs is obviously lower than that of CuGQD/PdNPs@PSi, demonstrating that the mimic-POD performance of CuGQD/PdNPs decreases after the destruction of PSi channel. The above steady-state kinetic results certificate for the first time that the confinement of PSi nanoscale platform endows the synergistic mimic-POD activity of dual nanozymes. Furthermore, NIR stimulation can obviously enhance the absorbance value of reaction system in the presence of PdNPs@PSi or CuGQD/PdNPs@PSi, while only marginally increase in CuGQD @PSi was observed (Figure 3e). The reason could be attributed to the heat caused by the photothermal response effect of PdNPs@PSi and CuGQD/PdNPs@PSi (Figure 3g). According to the steady-state kinetic test (Figure 3f; Table S2, Supporting Information), hyperthermia induced by NIR exposure can further accelerate the substrate binding rate (K_m value is 0.7726 мм), catalytic reaction rate (V_{max} value is 6.423×10^{-8} м s^{-1}), and the catalytic efficiency (V_{max}/K_m value is 8.313×10^{-5} s^{-1}) of CuGQD/PdNPs@PSi.

Usually, the generated •OH will be substantially depleted by the excess GSH in TME, thus we further explored whether CuGQD/PdNPs@PSi can consume excessive GSH. The reaction product (TNB) of 5,5′-dithiobis-(2-nitrobenzoic acid) (DTNB) with GSH has a typical absorption peak at 412 nm, therefore the residual GSH content can be monitored by the change of TNB absorption peak with reaction time. As shown in Figure 3g, compared with the control group and PSi group, the absorption peak of the reaction system at 412 nm decreases clearly when the system contains CuGQD@PSi or CuGQD/PdNPs@PSi, while the absorption value in the reaction system of PdNPs@PSi is almost unaltered. The Michaelis–Menton kinetics of CuGQD@PSi and CuGQD/PdNPs@PSi as mimic-GSHOx were also analyzed (Figure 3h,i). The K_m and V_{max} of CuGQD/PdNPs@PSi are calculated to be 0.4662 мм and 5.079×10^{-7} м s^{-1}, respectively. Overall, CuGQD/PdNPs@PSi (V_{max}/K_m value = 10.89×10^{-4} s^{-1}) performs three times catalytic efficiency than CuGQD@PSi (V_{max}/K_m value = 3.227×10^{-4} s^{-1}) (Table S3, Supporting Information). All results prove that the ability of CuGQD/PdNPs@PSi to oxidize the GSH is superior to that of CuGQD@PSi.

To elucidate the confinement effect of PSi, the steady-state kinetic analysis of the monoconfined nanozyme mixture containing CuGQD and PdNPs@PSi was performed as above using GSH as the substrate. Compared to CuGQD/PdNPs@PSi, the mixture has a higher K_m value (1.076 мм) and a lower V_{max} value (4.504×10^{-7} м s^{-1}) (Figure 3j). Meanwhile, the catalytic efficiency (V_{max}/K_m value) of the mixture is reduced by more than 60% against CuGQD/PdNPs@PSi. The above results also suggest that the dual confined nanozymes complex of CuGQD/PdNPs@PSi shows higher GSHOx catalytic activity than the monoconfined nanozyme mixture. In addition, the K_m value and V_{max} value of CuGQD/PdNPs were also calculated on the basis of the steady-state kinetics study. Compared with CuGQD/PdNPs@PSi, the K_m value of CuGQD/PdNPs increases to 0.9785 мм, the V_{max} value of CuGQD/PdNPs decreases to 4.143×10^{-7} м s^{-1}, and the V_{max}/K_m value drops to 4.234×10^{-4} s^{-1} (Figure S15, Table S3, Supporting Information), which proves that only PdNPs could not enhance the mimic-GSHOx activity of CuGQD without the assistance of PSi channel. Therefore, the excellent mimic-GSHOx activity of CuGQD/PdNPs@PSi may be ascribed to the nanoscale confinement of PSi, which enables PdNPs with the ability to accelerate electron transfer between CuGQD and substrates, eventually hastening the catalytic reaction. Additionally, the GSH scavenging ability of CuGQD/PdNPs@PSi represented by the absorbance value at 412 nm of reaction system further decreases under NIR stimulation, because the hyperthermia induced by PTT effect of PdNPs under NIR irradiation can improve the GSHOx-like catalytic activity in the CuGQD/PdNPs@PSi system (Figure 3k,l; Table S3, Supporting Information). By contrast, the absorbance value in CuGQD@PSi catalytic system cannot be significantly changed by NIR light because the CuGQD@PSi lack good photothermal properties (Figure 3k). Taken together, the PSi-based nanoscale confinement strategy allows the nanozyme composite to simultaneously exhibit synergistic and PTT-enhanced mimic-enzyme catalytic properties, which can be a potential nanoformulation for tumor therapy.

2.4. In Vitro Cytotoxicity of CuGQD/PdNPs@PSi

Further, the cytotoxicity of CuGQD/PdNPs@PSi on normal NIH3T3 cells and melanoma cells (B16-F10 cells) was evaluated by the CellTiter-Lumin assay. As shown in Figure S16a of the Supporting Information, the PSi, CuGQD@PSi, PdNPs@PSi, and CuGQD/PdNPs@PSi could not cause obvious toxicity to NIH3T3 cells. After application of NIR stimulation, the viability of NIH3T3 cells treated with different concentrations of the four nanomaterials could still maintain above 82% (Figure S16b, Supporting Information). By contrast, the cell viability of B16-F10 shows a dose-dependent behavior in CuGQD/PdNPs@PSi group, and the cell-killing rate (≈70%) is significantly higher than that of the PSi group, CuGQD@PSi group, and PdNPs@PSi group at the same concentration (**Figure 4**a), supporting that CuGQD/PdNPs@PSi possess synergistic ability to suppress of tumor cell growth. Under exposure to 808 nm, the B16-F10 cell viability further reduce to only 10% in the CuGQD/PdNPs@PSi group with the concentration of 500 μg mL^{-1} (Figure 4b), indicating the additional photothermal

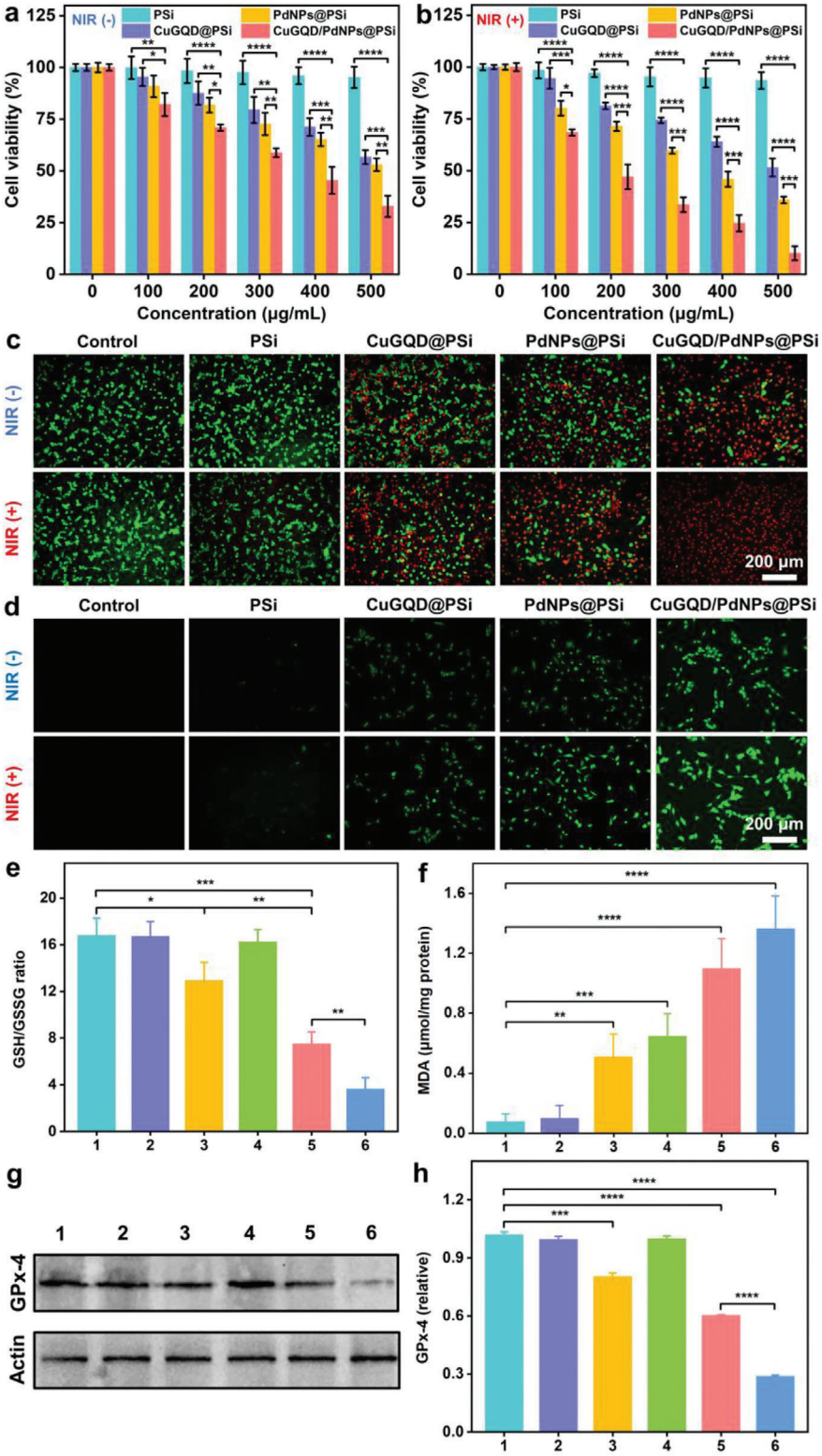

Figure 4. Cell viability of B16-F10 cells against PSi, CuGQD@PSi, PdNPs@PSi, and CuGQD/PdNPs@PSi at different concentrations a) without or b) with NIR irradiation (808 nm, 1.0 W cm^{-2}, 5 min). c) Fluorescence images of B16-F10 cells with various treatments using Calcein-AM and PI costaining. d) Detection of hydroxyl radical in B16-F10 cells after different treatments using DCFH-DA as the fluorescent probe. e) The GSH/GSSG ratio and f) MDA production of B16-F10 cells with different treatments. g) Western blots results and h) quantification of the GPx-4 expression level in B16-F10 cells following different treatments. Group 1: control; 2: PSi; 3: CuGQD@PSi; 4: PdNPs@PSi; 5: CuGQD/PdNPs@PSi; 6: CuGQD/PdNPs@PSi + NIR. * represents $P < 0.05$, ** represents $P < 0.01$, *** represents $P < 0.001$, and **** represents $P < 0.0001$. The number of parallel detection $n = 3$.

characteristics of CuGQD/PdNPs@PSi can further improve the tumor cells killing efficiency. Similar results are observed in the fluorescent staining of living and dead cells (Figure 4c). In addition, the production of ROS in tumor cells was detected by DCFH-DA fluorescent probe. As shown in Figure 4d, stronger green fluorescence is observed in the CuGQD/PdNPs@PSi group in comparison with the CuGQD@PSi group and PdNPs@PSi group, suggesting synergistic mimic-POD catalytic activity caused by interplay of dual nanozymes confined in PSi is also reflected at the cellular level. Simultaneously, the most pronounced green fluorescence is shown in the CuGQD/PdNPs@PSi group with NIR irradiation, indicating that photothermal stimulation could enhance the mimic-POD performance of CuGQD/PdNPs@PSi in B16-F10 cells. The superior POD-like performance of CuGQD/PdNPs@PSi can effectively promote the accumulation of LPO. However, this bioprocess would be quickly blocked by the high level of GSH present in the tumor cells. Depending on the GSH-depleting capacity of CuGQD/PdNPs@PSi group, the GSH/GSSG ratio in tumor cells treated with CuGQD/PdNPs@PSi is lower than that of CuGQD@PSi and PdNPs@PSi. Furthermore, the performance of consume GSH of CuGQD/PdNPs@PSi could be further improved after application of 808 nm light (Figure 4e). The above results indicate that the prepared CuGQD/PdNPs@PSi possess the synergistic and PTT-enhanced mimic-GSHOx catalytic property in vitro. Consequently, the CuGQD/PdNPs@PSi + NIR light induced the highest malondialdehyde (MDA) level, reflecting that the prepared CuGQD/PdNPs@PSi could cause high accumulation of LPO in B16-F10 cells (Figure 4f), and result in the subsequent ferroptosis, as evidenced by the apparently reduced expression of GPx-4 (Figure 4g,h; Figure S17, Supporting Information). These *in vitro* results confirm that dual nanozymes loading in PSi host can lead to enhanced POD and GSHOx performance, thereby inducing effective intracellular ferroptosis that can be further enhanced by hyperthermic stimulation.

2.5. Fabrication and Characterization of CuGQD/PdNPs@PSi MNs

Recently, MNs loaded with nanocomplex have been reported for ferroptosis-mediated synergistic wound therapy.[53] In addition, the antibacterial infection effect of MNs encapsulated with photothermal nanozyme have also been proven.[54] Encouraged by the previous works and remarkable nanocatalytic performance of the CuGQD/PdNPs@PSi in vitro, we further integrated CuGQD/PdNPs@PSi into the ultralive hyaluronic acid (HA) matrix to develop a dissolvable microneedle patch specifically for melanoma treatment. HA with good biocompatible and water-solubility was employed as the matrix of MNs.[55] As shown in **Figure 5**a, CuGQD/PdNPs@PSi MNs were fabricated by the step-casting method. Firstly, the tip of PDMS mold was filled with HA and CuGQD/PdNPs@PSi mixture through centrifugation, then the mold backing was formed by dropping the pure HA solution into the mold followed by centrifugation. Finally, the CuGQD/PdNPs@PSi MNs were obtained by holding the microneedle edge area with tweezers and slowly separating it from the mould after drying overnight. As shown in Figure 5b,c, the arranged neatly needle of CuGQD/PdNPs@PSi MNs has an intact pyramid shape with a needle tip height of 650 μm and an array size of 10 × 10. Meanwhile, elemental mapping images show the presence of Si, Pd, and a small amount of Cu elements in the tip, indicating that the CuGQD/PdNPs@PSi have been successfully integrated into the microneedles (Figure 5d). Furthermore, we dissolved the microneedles in water and collected the nanocomplex by centrifugation and freeze-drying. Weight analysis show that 1.033 ± 0.1155 mg (n = 3) of CuGQD/PdNPs@PSi could be loaded into each microneedle patch.

In addition, the average mechanical strength of blank HA microneedles at 400 μm displacement is 0.2853 ± 0.02366 N per needle (n = 3). By contrast, the average mechanical strength of microneedles loaded with CuGQD/PdNPs@PSi significantly increases to be 0.9735 ± 0.01553 N per needle at 400 μm displacement (Figure 5e), indicating that the mechanical properties of microneedles are greatly enhanced by the introduction of CuGQD/PdNPs@PSi. As a result, mechanical properties of CuGQD/PdNPs@PSi MNs are sufficient to penetrate the epidermal layer.[56,57] As shown in Figure S18 of the Supporting Information, CuGQD/PdNPs@PSi MNs could bend but not break after the compression test.

We subsequently evaluated the in vitro skin insertion ability of CuGQD/PdNPs@PSi MNs by piercing the excised porcine skin. After pressing CuGQD/PdNPs@PSi MNs into porcine skin for 60 s, the microneedle tip completely dissolves (Figure S19, Supporting Information), and clear black spots of 10 × 10 arrays corresponding to the MNs array could be observed on the porcine skin surface via an optical microscope (Figure S20a, Supporting Information). The hematoxylin and eosin (H&E) staining assays reveal that CuGQD/PdNPs@PSi MNs could pierce the stratum corneum to form microchannels (Figure S20b, Supporting Information). As shown in Figure 5f, Si, Pd, and Cu elements could be released rapidly after CuGQD/PdNPs@PSi MNs insertion into porcine skin, and the release equilibrium could be reached in only 60 s. We then carried out an i*n vivo* microneedle insertion performance test, the microchannels left by the CuGQD/PdNPs@PSi MNs penetrating the nude mouse skin could also be clearly visualized (Figure S21a, Supporting Information). The H&E staining assays further confirm that CuGQD/PdNPs@PSi MNs can effectively penetrate the mice skin barrier for cargo delivery (Figure S21b, Supporting Information). Besides, the CuGQD/PdNPs@PSi still maintains excellent photothermal properties after being integrated into the microneedle (Figure 5g).

After storing the microneedles for three months at room temperature and dry conditions, CuGQD/PdNPs@PSi extracted from the microneedle still maintains dispersed nanostructure. Compared to freshly prepared CuGQD/PdNPs@PSi, no significant changes in particle size could be observed (Figure S22a, Supporting Information), confirming the stability of CuGQD/PdNPs@PSi in microneedles. In addition, the photothermal response of CuGQD/PdNPs@PSi MNs after three months could be maintained at 99.31% of its original value (Figure S22b, Supporting Information). Meanwhile, compared with fresh CuGQD/PdNPs@PSi MNs, the ability of CuGQD/PdNPs@PSi MNs after three months of storage could still remain above 98.5% inhibit rate to the growth of B16-F10 cells with NIR stimulation (Figure S22c, Supporting

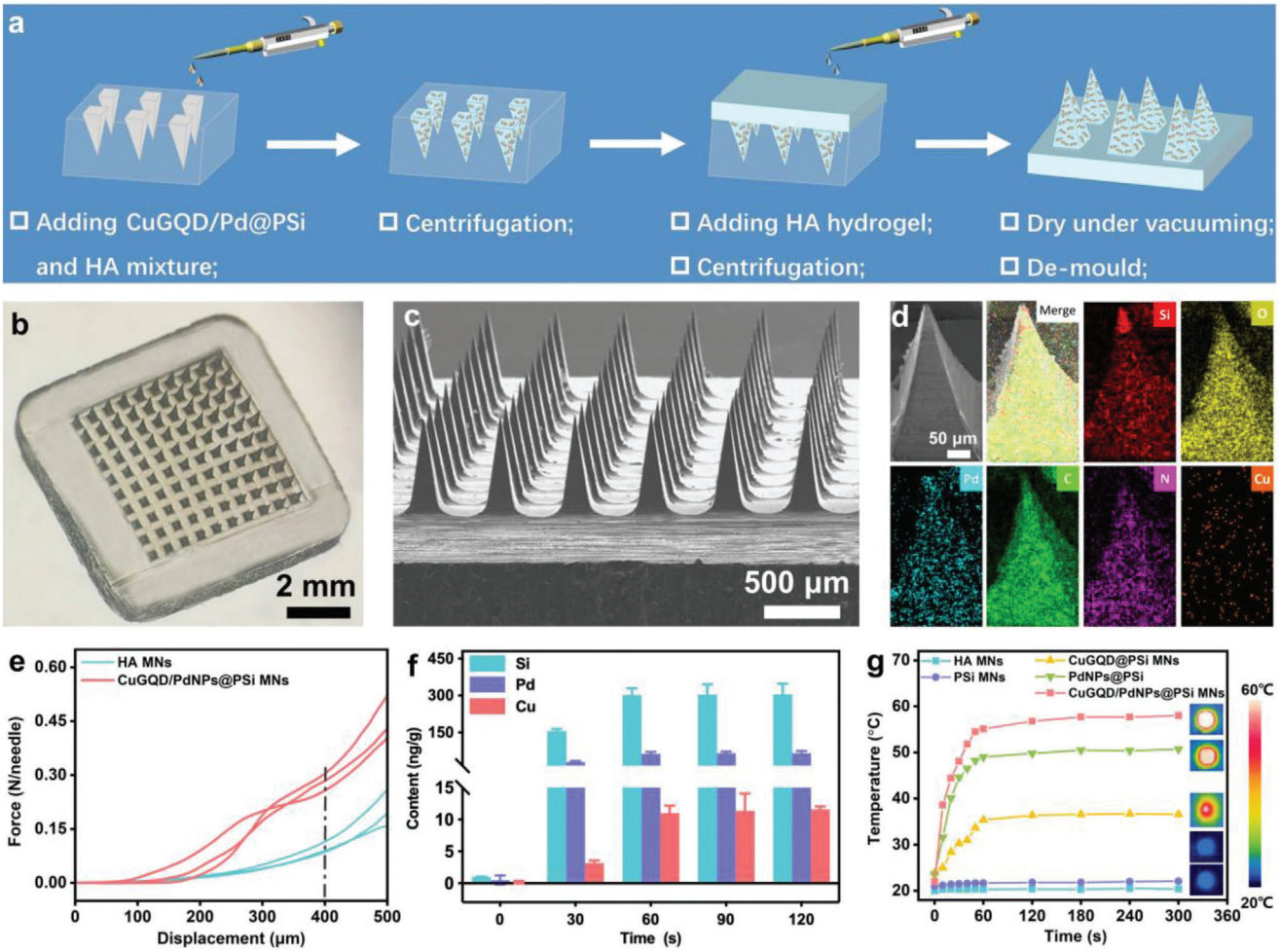

Figure 5. Fabrication and characterization of CuGQD/PdNPs@PSi MNs. a) Flow chart of CuGQD/PdNPs@PSi MNs. b) Stereomicroscope image and c) SEM image of CuGQD/PdNPs@PSi MNs. d) Elemental mappings of CuGQD/PdNPs@PSi MNs. e) Mechanical strength tests of pure HA MNs and CuGQD/PdNPs@PSi MNs ($n = 3$). f) Release of Si, Pd, and Cu elements from CuGQD/PdNPs@PSi MNs after inserting into the porcine skin for different times. g) The photothermal response curve of different MNs under NIR irradiation, insets represent thermal images of HA MNs loaded with different materials.

Information). All these results demonstrate the good storage stability of CuGQD/PdNPs@PSi in microneedle and the potential for practical application.

2.6. In Vivo Therapeutic Performance of CuGQD/PdNPs@PSi MNs

The model of nude mice bearing B16-F10 tumors was established to evaluate the antitumor properties of CuGQD/PdNPs@PSi MNs in vivo (**Figure 6**a). According to the above in vitro therapeutic effects, the exogenous hyperthermia induced by NIR irradiation can dramatically promote the nanocatalytic efficiency of CuGQD/PdNPs@PSi, therefore the next experiments are all stimulated by NIR light.

In this study, we used ultralive HA with molecular weight less than 5000. Ultralive hyaluronic acid can inhibit the aggregation of highly overexpressed glycoprotein CD44 on the surface of cancer cells, which enhances the permeability of the drug delivery and can be effectively absorbed by the cells. Meanwhile, ultralive HA has been reported to increase the permeability of nanomaterials to cancer cells, thus enabling more effective uptake by cancer cells.[58,59] Ultralive HA-based microneedles have been used to load photosensitizers for the photodynamic treatment of melanoma.[60,61] As a control experiment, the effect of HA MNs application on melanoma growth in vivo in the absence of nanomaterial loading was investigated. The tumor-bearing nude mice were randomly divided into NIR group and NIR + HA MNs group ($n = 4$) once the tumor volume reached 100 mm^3. After 14 days of treatment, the tumors of nude mice in the NIR-only stimulation group grow in a completely uncontrollable manner (tumor volume = 2220 mm^3). With the simultaneous application of HA microneedle and NIR stimulation, the tumor growth trend could be slightly suppressed with tumor volume of 1840 mm^3 (the tumor growth inhibition rate (TGI) is ≈11.2%) (Figure S23, Supporting Information). The above results suggest that one-time application of HA MNs alone is not effective in inhibiting melanoma progression.

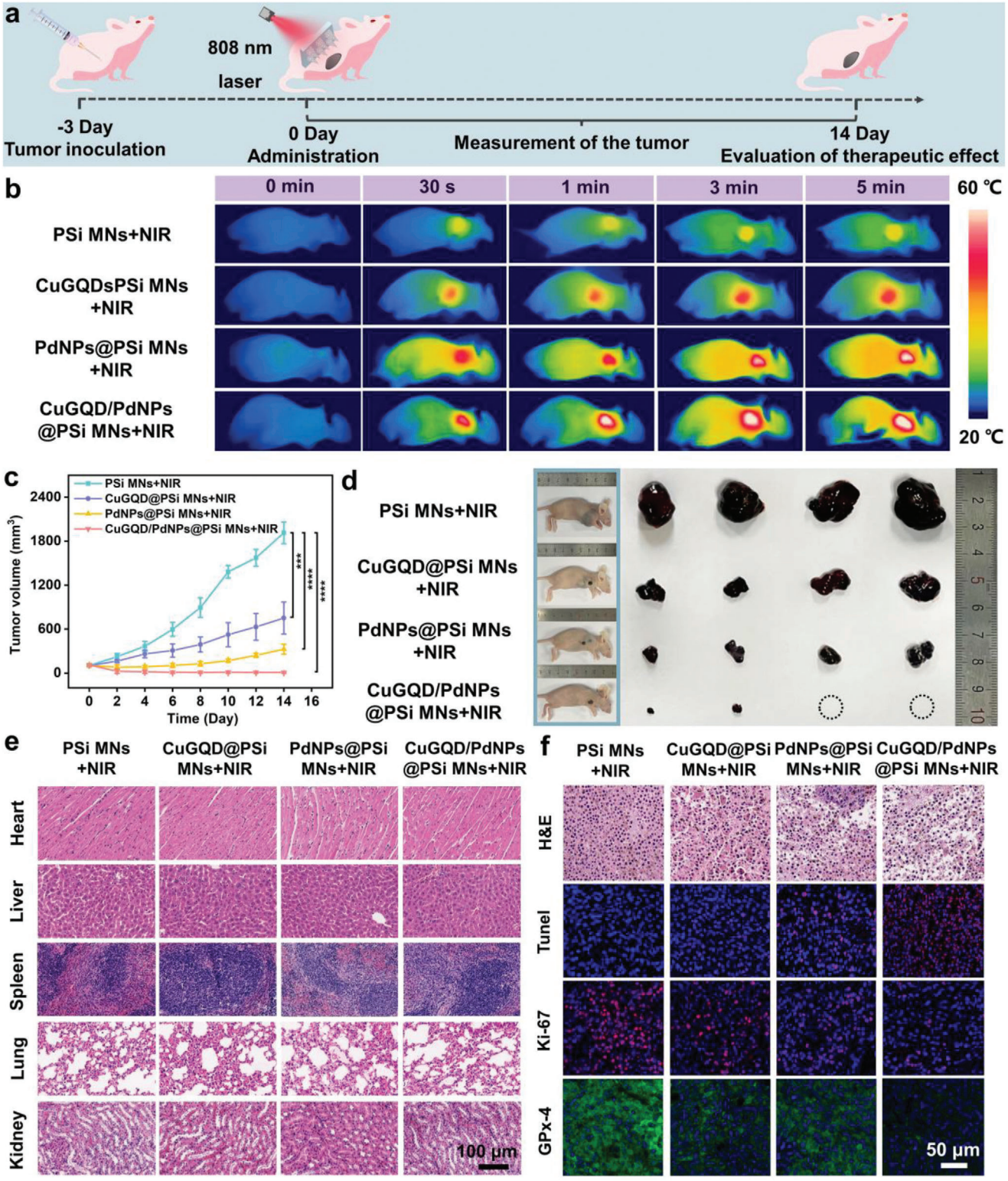

Figure 6. a) Schematic illustration of melanoma treatment in vivo. b) Thermal images of tumor-bearing mice in different treatment processes. c) The tumor volume curve of different groups. d) Photographs of tumor-bearing mice (right) and tumor (left) after 14 days of different treatments. e) H&E staining analysis of main organs from tumor-bearing mice after different treatments. f) Tumor section analysis by H&E, TUNEL, Ki67, and GPx-4. * represents $P < 0.05$, ** represents $P < 0.01$, *** represents $P < 0.001$, and **** represents $P < 0.0001$, $n = 4$.

Thereafter, we further evaluated the effect of nanomaterial-loaded MNs on melanoma growth in vivo under NIR stimulation. When the tumor volume reached 100 mm^3, these tumor-bearing nude mice were also randomly divided into four groups (n = 4): i) NIR + PSi MNs group, ii) NIR + CuGQD@PSi MNs group, iii) NIR + PdNPs@PSi MNs group, and iv) NIR + CuGQD/PdNPs@PSi MNs group. When exposed to NIR irradiation, the temperature of mice treated with PSi MNs or CuGQD@PSi MNs could not exceed 45 °C, while the local tumor temperature of mice treated with PdNPs@PSi MNs and CuGQD/PdNPs@PSi MNs increase to 51 and 56 °C. It should be noted that the tumor cells can be inhibited and tumor growth can be inhibited at a local temperature of ≈53 °C without permanent burn damage (Figure 6b).[62] As shown in Figure 6c, the tumor of mice treated with PSi MNs + NIR continues to grow, reaching 1900 mm^3 on the 14th day, suggesting undesirable inhibition of tumor growth. Meanwhile, the tumor volume in CuGQD@PSi MNs + NIR group could reach 750 mm^3 on the 14th day, indicating that the therapy result is not satisfactory even through the regulation of endogenous H_2O_2 and GSH can partially inhibit tumor growth. By contrast, the tumor volume of the PdNPs@PSi MNs + NIR group can only reach 300 mm^3 after 14 days of treatment with a TGI value of 86.3%, suggesting that PTT-enhanced POD reaction could slow down melanoma development in vivo. Notably, the majority of tumors in the CuGQD/PdNPs@PSi MNs + NIR group have shrunk in size or vanished completely after two weeks and the TGI value can be as high as 98.8%. According to the photographs of mice with different treatments (Figure 6d left), the CuGQD/PdNPs@PSi MNs + NIR group only leaves a small scab, while the presence of tumors in other three groups could be obviously observed. The photographs of exfoliated tumor tissues and the average weight of tumors in different groups also demonstrate the superior therapeutic effect of CuGQD/PdNPs@PSi MNs under NIR irradiation (Figure 6d right; Figure S24, Supporting Information). Aiming to explore the distribution of nanosystem in vivo after microneedle administration, CuGQD/PdNPs@PSi were labeled with red fluorescent dye and then incorporated into microneedles. As shown in Figure S25a,b of the Supporting Information, the fluorescence signal was mainly concentrated at the tumor site rather than other organs after 1 h of administration, indicating that the microneedles could indeed deliver the CuGQD/PdNPs@PSi to the tumor site.

The degradation and metabolism of nanomaterials in vivo were also been studied. After 1 day of administration, accumulation of CuGQD/PdNPs@PSi could be observed at tumor site, as well as in liver, spleen and kidney, indicating that CuGQD/PdNPs@PSi have entered the circulation in vivo (Figure S26, Supporting Information). The accumulation of Si, Pd, Cu elements in the organs significantly decreases after 14 days, because the PSi carrier is biodegradable and allow the loaded dual nanozymes to be subsequently excreted and removed.[33] Moreover, no pathological abnormalities are observed in H&E staining images of major organs (heart, liver, spleen, lung, kidney) (Figure 6e). Meanwhile, barely abnormal weight changes could be found in several different groups during the treatment (Figure S27, Supporting Information). These results indicate that the designed microneedle delivery system of nanocomplex is biosafety and biocompatibility. In addition, compared with the control group, the blood routine indexes of the CuGQD/PdNPs@PSi MNs + NIR group after one week and two weeks of administration have no significant fluctuation (Figure S28, Supporting Information), demonstrating the application of CuGQD/PdNPs@PSi MNs could not bring the risk of acute infection, hemolytic anemia, and other syndromes.

Further, we explored the possible mechanism of antitumor by histological analysis. As shown in Figure 6f, the H&E staining of tumor tissues in the CuGQD/PdNPs@PSi MNs + NIR group displays the highest degree of apoptosis in four groups with different treatments, including fragmentation and tumor cell lysis. The immunofluorescence staining of terminal deoxynucleotidyl transferase dUTP nick-end labeling (TUNEL) assays and Ki-67 assays also verify that the CuGQD/PdNPs@PSi MNs + NIR group display the highest activity in killing cancer cells and inhibiting their proliferation among the four treatment groups. The immunofluorescence staining results of GPx-4 in the CuGQD/PdNPs@PSi MNs + NIR group show the most significant downregulation in contrast to the other groups, revealing that the excellent antitumor effect could be attributed to ferroptosis induced by the decrease in the expression level of GPx-4. All the above results indicate that CuGQD/PdNPs@PSi MNs under NIR irradiation possess desirable tumor therapeutic performance in vivo.

3. Conclusion

In this work, we constructed CuGQD/PdNPs@PSi-integrated MNs for synergistic nanocatalytic therapy to induce ferroptosis against melanoma. The as-prepared CuGQD/PdNPs@PSi not only display superior photothermal performance but also show synergistic and PTT-enhanced bifunctional mimic enzyme properties. The special synergistic mimic-POD and GSHOx performance could be attributed to the confinement effect of PSi host. Upon TME stimulation, CuGQD/PdNPs@PSi exhibit excellent ROS-scavenging and GSH-depleting capabilities. Moreover, CuGQD/PdNPs@PSi demonstrate enhanced mimic-POD and GSHOx activities with hyperthermia brought from NIR irradiation could trigger more efficient ferroptosis pathway in vitro. In order to better deliver the prepared nanocomposite to the diseased sites of melanoma, we integrated CuGQD/PdNPs@PSi into MNs, which are characterized by allowing loaded cargoes to access to subcutaneous tissues in a minimally invasive and painless manner. This work first proposed a new idea for enhancing the performance of multi-nanozyme by exploiting the spatial confinement effect of PSi host. The synergistic catalytic properties of multi-nanozyme are expected to overcome the negative effects of complex TME to achieve efficient and universal stimulated response tumor therapy. Further, we have integrated the multi-nanozyme therapy into MNs administration, resulting in effective delivery of synergistic nanozymes to superficial melanoma and thereby efficient elimination of tumor cells via the ferroptosis with marginal side effects. Taken together, microneedle integration of PSi-based nanozyme complex will be a pervasive platform in various clinical applications.

Supporting Information

Supporting Information is available from the Wiley Online Library or from the author.

Acknowledgements

The authors acknowledged the financial support by the National Natural Science Foundation of China (No. 22274138;No. 22374130). The authors also appreciated the Laboratory Animal Center of Zhejiang University (Hangzhou, China) and were supervised and approved by the Animal Ethics Committee of Zhejiang University (ZJU20220361).

Conflict of Interest

The authors declare no conflict of interest.

Data Availability Statement

The data that support the findings of this study are available from the corresponding author upon reasonable request.

Keywords

dual nanozymes, melanoma treatment, microneedles, porous silicon, synergistic nanocatalysis induced ferroptosis

Received: July 16, 2023
Revised: August 19, 2023
Published online:

[1] R. Gordon, *Semin. Oncol. Nurs.* **2013**, *29*, 160.
[2] J. K. Cullen, J. L. Simmons, P. G. Parsons, G. M. Boyle, *Adv. Drug Delivery Rev.* **2020**, *153*, 54.
[3] H. G. Das, L. Bräutigam, L. Pudelko, R. Tuominen, V. Höiom, I. Almlöf, V. Rajagopal, J. Hansson, T. Helleday, S. Egyházi Brage, U. Warpman Berglund, *Cell Death Differ.* **2020**, *27*, 2081.
[4] L. An, P. Zhang, W. Shen, X. Yi, W. Yin, R. Jiang, C. Xiao, *Bioact. Mater.* **2021**, *6*, 1365.
[5] D. C. Whiteman, A. C. Green, C. M. Olsen, *J. Invest. Dermatol.* **2016**, *136*, 1161.
[6] J. R. Etzkorn, J. M. Sharkey, J. W. Grunyk, T. M. Shin, J. F. Sobanko, C. J. Miller, *J. Am. Acad. Dermatol.* **2017**, *77*, 341.
[7] V. Nikolaou, A. Stratigos, D. Bafaloukos, A. Katsambas, *Clin. Dermatol.* **2013**, *31*, 257.
[8] T. Achkar, A. A. Tarhini, *J. Hematol. Oncol.* **2017**, *10*, 88.
[9] X. Xu, L. Yuan, Y. Gai, Q. Liu, L. Yin, Y. Jiang, Y. Wang, Y. Zhang, X. Lan, *J. Exp. Clin. Cancer Res.* **2018**, *37*, 306.
[10] H. Wei, L. Gao, K. Fan, J. Liu, J. He, X. Qu, S. Dong, E. Wang, X. Yan, *Nano Today* **2021**, *40*, 101269.
[11] H. Deng, W. Yang, Z. Zhou, R. Tian, L. Lin, Y. Ma, J. Song, X. Chen, *Nat. Commun.* **2020**, *11*, 4951.
[12] W. J. Ho, E. M. Jaffee, L. Zheng, *Nat. Rev. Clin. Oncol.* **2020**, *17*, 527.
[13] S. Dong, Y. Dong, B. Liu, J. Liu, S. Liu, Z. Zhao, W. Li, B. Tian, R. Zhao, F. He, S. Gai, Y. Xie, P. Yang, Y. Zhao, *Adv. Mater.* **2022**, *34*, 2107054.
[14] J. Chen, X. Liu, G. Zheng, W. Feng, P. Wang, J. Gao, J. Liu, M. Wang, Q. Wang, *Small* **2022**, *19*, 2205924.
[15] L. Gao, J. Zhuang, L. Nie, J. Zhang, Y. Zhang, N. Gu, T. Wang, J. Feng, D. Yang, S. Perrett, X. Yan, *Nat. Nanotechnol.* **2007**, *2*, 577.
[16] H. Sun, Y. Zhou, J. Ren, X. Qu, *Angew. Chem., Int. Ed.* **2018**, *57*, 9224.
[17] E. Ju, K. Dong, Z. Chen, Z. Liu, C. Liu, Y. Huang, Z. Wang, F. Pu, J. Ren, X. Qu, *Angew. Chem., Int. Ed.* **2016**, *55*, 11467.
[18] M. Ma, Z. Liu, N. Gao, Z. Pi, X. Du, J. Ren, X. Qu, *J. Am. Chem. Soc.* **2020**, *142*, 21702.
[19] N. Singh, M. A. Savanur, S. Srivastava, P. D'Silva, G. Mugesh, *Angew. Chem.* **2017**, *129*, 14455.
[20] A. A. Vernekar, D. Sinha, S. Srivastava, P. U. Paramasivam, P. D'Silva, G. Mugesh, *Nat. Commun.* **2014**, *5*, 5301.
[21] X. Meng, D. Li, L. Chen, H. He, Q. Wang, C. Hong, J. He, X. Gao, Y. Yang, B. Jiang, G. Nie, X. Yan, L. Gao, K. Fan, *ACS Nano* **2021**, *15*, 5735.
[22] M. Chang, Z. Hou, M. Wang, C. Yang, R. Wang, F. Li, D. Liu, T. Peng, C. Li, J. Lin, *Angew. Chem., Int. Ed.* **2021**, *60*, 12971.
[23] M. Tang, Y. Shi, L. Lu, J. Li, Z. Zhang, J. Ni, W. Wang, Y. Zhang, T. Sun, Z. Wu, *Chem. Eng. J.* **2022**, *449*, 137847.
[24] S. Dong, Y. Dong, T. Jia, S. Liu, J. Liu, D. Yang, F. He, S. Gai, P. Yang, J. Lin, *Adv. Mater.* **2020**, *32*, 2002439.
[25] Y. Wang, K. Wang, J. Zhao, X. Liu, J. Bu, X. Yan, R. Huang, *J. Am. Chem. Soc.* **2013**, *135*, 4799.
[26] S. Liu, Y. Yin, M. Wu, K. S. Hui, K. N. Hui, C. Y. Ouyang, S. C. Jun, *Small* **2019**, *15*, 1900524.
[27] S. Gao, H. Lin, H. Zhang, H. Yao, Y. Chen, J. Shi, *Adv. Sci.* **2018**, *6*, 1801733.
[28] Y. Jin, Y. Yang, W. Duan, X. Qu, J. Wu, *ACS Appl Mater Interfaces* **2021**, *13*, 16127.
[29] E. Anglin, L. Cheng, W. Freeman, M. J. Sailor, *Adv. Drug Delivery Rev.* **2008**, *60*, 1266.
[30] W. Duan, Y. Jin, Y. Cui, F. Xi, X. Liu, F. Wo, J. Wu, *Biomaterials* **2021**, *272*, 120772.
[31] J. H. Park, L. Gu, G. V. Maltzahn, E. Ruoslahti, S. N. Bhatia, M. J. Sailor, *Nat. Mater.* **2009**, *8*, 331.
[32] Y. Cui, Y. Jin, X. Chen, J. Wu, *ACS Sens.* **2018**, *3*, 1439.
[33] Y. Cui, W. Duan, Y. Jin, F. Wo, F. Xi, J. Wu, *ACS Sens.* **2020**, *5*, 2096.
[34] X. Chen, F. Wo, Y. Jin, J. Tan, Y. Lai, J. Wu, *ACS Nano* **2017**, *11*, 7938.
[35] W. Duan, X. Liu, J. Zhao, Y. Zheng, J. Wu, *ACS Appl Mater Interfaces* **2022**, *14*, 48368.
[36] T. Kim, G. B. Braun, Z. She, S. Hussain, E. Ruoslahti, M. J. Sailor, *ACS Appl. Mater. Interfaces* **2016**, *8*, 30449.
[37] E. J. Kwon, M. Skalak, A. Bertucci, G. Braun, F. Ricci, E. Ruoslahti, M. J. Sailor, S. N. Bhatia, *Adv. Mater.* **2017**, *29*, 1701527.
[38] A. Cifuentes-Rius, A. Ivask, E. Sporleder, I. Kaur, Y. Assan, S. Rao, D. Warther, C. A. Prestidge, J. O. Durand, N. H. Voelcker, *Small* **2017**, *13*, 1701201.
[39] F. Zhang, A. Correia, E. Mäkilä, W. Li, J. Salonen, J. J. Hirvonen, H. Zhang, H. A. Santos, *ACS Appl. Mater. Interfaces* **2017**, *9*, 10034.
[40] Y. Cui, W. Duan, Y. Jin, F. Wo, F. Xi, J. Wu, *Acta Biomater.* **2021**, *131*, 544.
[41] L. Li, H. Liu, J. Bian, X. Zhang, Y. Fu, Z. Li, S. Wei, Z. Xu, X. Liu, Z. Liu, D. Wang, D. Gao, *Chem. Eng. J.* **2020**, *397*, 125438.
[42] J. Cen, Y. Huang, J. Liu, Y. Liu, *J. Mater. Chem. B* **2022**, *10*, 10027.
[43] S. Sun, Q. Chen, Z. Tang, C. Liu, Z. Li, A. Wu, H. Lin, *Angew. Chem., Int. Ed.* **2020**, *59*, 21041.
[44] J. Xi, G. Wei, L. An, Z. Xu, Z. Xu, L. Fan, L. Gao, *Nano Lett.* **2019**, *19*, 7645.
[45] R. Amarnani, P. Shende, *Biomed. Microdevices* **2022**, 24, 4.
[46] H. Cheng, M. Liu, X. Du, J. Xu, Y. Zhai, J. Ji, S. He, G. Zhai, *J. Drug Delivery Sci. Technol.* **2019**, *50*, 18.
[47] Y. Yan, J. Gong, J. Chen, Z. Zeng, W. Huang, K. Pu, J. Liu, P. Chen, *Adv. Mater.* **2019**, *31*, 1808283.
[48] R. Hu, Y. Fang, M. Huo, H. Yao, C. Wang, Y. Chen, R. Wu, *Biomaterials* **2019**, *206*, 101.
[49] G. Song, Y. Sun, T. Liu, X. Zhang, Z. Zeng, R. Wang, P. Li, C. Li, G. Jiang, *Chem. Eng. J.* **2021**, *426*, 130790.
[50] C. Wang, Y. Li, W. Yang, L. Zhou, S. Wei, *Adv. Healthcare Mater.* **2021**, *10*, 2100601.
[51] L. Guo, J. Bai, C. Li, Q. Meng, H. Liang, W. Sun, H. Li, H. Liu, *Appl. Surf. Sci.* **2013**, *283*, 107.
[52] Y. Li, L. Xu, B. Xu, Z. Mao, H. Xu, Y. Zhong, L. Zhang, B. Wang, X. Sui, *ACS Appl. Mater. Interfaces* **2017**, *9*, 17155.

[53] B. Zhao, W. Guo, X. Zhou, Y. Xue, T. Wang, Q. Li, L. Tan, L. Shang, *Adv. Funct. Mater.* **2023**, *33*, 2300575.
[54] W. Zhu, J. Mei, X. Zhang, J. Zhou, D. Xu, Z. Su, S. Fang, J. Wang, X. Zhang, C. Zhu, *Adv. Mater.* **2022**, *34*, 2207961.
[55] U. Freudenberg, Y. Liang, K. L. Kiick, C. Werner, *Adv. Mater.* **2016**, *28*, 8861.
[56] T. Waghule, G. Singhvi, S. K. Dubey, M. M. Pandey, G. Gupta, M. Singh, K. Dua, *Biomed. Pharmacother.* **2019**, *109*, 1249.
[57] Z. Tong, J. Zhou, J. Zhong, Q. Tang, Z. Lei, H. Luo, P. Ma, X. Liu, *ACS Appl. Mater. Interfaces* **2018**, *10*, 20014.
[58] C. Deng, Q. Zhang, Y. Fu, X. Sun, T. Gong, Z. Zhang, *ACS Appl. Mater. Interfaces* **2017**, *9*, 1280.
[59] Y. Kang, W. Sun, S. Li, M. Li, J. Fan, J. Du, X. J. Liang, X. Peng, *Adv. Sci.* **2019**, *6*, 1900716.
[60] Q. Bian, L. Huang, Y. Xu, R. Wang, Y. Gu, A. Yuan, X. Ma, J. Hu, Y. Rao, D. Xu, H. Wang, J. Gao, *ACS Nano* **2021**, *15*, 19468.
[61] Y. Li, G. He, L. H. Fu, M. R. Younis, T. He, Y. Chen, J. Lin, Z. Li, P. Huang, *ACS Nano* **2022**, *16*, 17298.
[62] Q. Lei, D. He, L. Ding, F. Kong, P. He, J. Huang, J. Guo, C. J. Brinker, G. Luo, W. Zhu, Y. Yu, *Adv. Funct. Mater.* **2022**, *32*, 2113269.